Received 26 January 2022; revised 4 March 2022; accepted 9 March 2022. Date of publication 14 March 2022; date of current version 24 March 2022.

Digital Object Identifier 10.1109/OJAP.2022.3159279

Sensor Arrangement in Through-the Wall Radar Imaging

MARIA ANTONIA MAISTO [1,2] (Member, IEEE), MEHDI MASOODI [1,2], ROCCO PIERRI [1,2], AND RAFFAELE SOLIMENE [1,2] (Senior Member, IEEE)

[1] Diparitmento di Ingegneria, Universit degli Studi della Campania—Luigi Vanvitelli, 81031 Aversa, Italy

[2] Consorzio Nazionale Interuniversitario per le Telecomunicazioni, 43124 Parma, Italy

CORRESPONDING AUTHOR: M. A. MAISTO (e-mail: mariaantonia.maisto@unicampania.it)

ABSTRACT In this paper, the problem of how to spatially sample the scattered field in microwave through-the wall imaging is addressed. To this end, a two-dimensional scalar configuration for a three-layered back-ground medium is considered under a linearized scattering model. The aim is to collect as low as possible measurements by maintaining the same performance in the reconstructions. Accordingly, the number and the positions of the spatial measurement points are determined so that the point-spread function of the resulting semi-discrete problem approximates well the one of the ideal continuous case (i.e., when data space is not sampled at all). It is shown that the resulting measurement spatial positions must be non-uniformly arranged across the measurement domain and their number is generally much lower than the one returned by some literature sampling criteria. Also, the measurement points can be analytically determined by taking into account the geometrical parameters as well as the wall features. Numerical examples are included to check the theoretical arguments.

INDEX TERMS Through-the wall radar imaging, nonuniform sampling, sampling methods, migration inversion.

I. INTRODUCTION

THROUGH wall radar imaging (TWRI) exploits the electromagnetic wave capability to penetrate through non-metallic obstacles to detect and localize targets hidden behind them. This kind of problems find application in both military and civilian contexts and hence has recently triggered a great deal of research efforts [1]. Many reconstruction algorithms have been developed in literature, such as inverse filtering [2], delay-and-sum beam-forming [3], [4], back-projection [5], contrast source inversion [6], and diffraction tomography (DT) [7], [8]. They mainly differ for the computational effort, processing speed, stability against the noise and also the presence of possible spurious targets inside the image region.

Usually, high-resolution reconstructions require wide-band (UWB) signals and large measurement apertures [9]. This can lead to long data collection time and a huge amount of data. Therefore, if targets move during the acquisition/processing stages blurred reconstructions are obtained.

Accordingly, reducing the number of measurements, by possibly maintaining the achievable performance, is of great importance and a number of strategies have been proposed in literature. In [10]–[12] data reduction is achieved by exploiting a priori information concerning the sparsity of the scattering scene and the consequent application of compressive sensing (CS) based algorithms. In fact, under certain conditions, CS works fine by using a number of data which is below the Nyquist limit [13], [14]. However, a l_1 norm minimization must be run and, what is more, the sampling strategy to ensure the strict validity of the CS paradigm is not often easy to find [15]. Other approaches cast the problem as a sensor' selection problem [16]. The latter requires an exhaustive exploration among all possible measurement point arrangements and is therefore combinatorial in nature. To overcome the related huge computational burden, many methods, based on convex optimization, greedy methods and heuristics, have been proposed [17], [18]. However, such methods select the measurement points by running iterative

procedures and generally require a priori information on the problem number of degrees of freedom (NDF) [19]–[22].

Recently, we have introduced a sampling strategy which relies on the mathematical properties of the linearized scattering operator [24], [25] and is conceived to approximate the ideal point-spread function, that is the one obtained in the case the data are continuously collected, corresponding to a migration-like inversion method [26]. The main merit of such an approach is that the sampling points are analytically determined and shows a clear dependence on the configuration parameters. Hence, as opposed to approaches mentioned above, the proposed sampling strategy does not require information concerning the sparsity of the solution and NDF, and does not require to run iterative procedures.

In the previous contributions, under a mono-static/multi-frequency scalar 2D scattering configuration, we considered the cases of homogeneous and two half-space back-ground media [24], [25]. However, the method is general and can be adapted to a more complex back-ground medium. Here, we just extend the analysis to a three-layered background medium, which is relevant in TWRI applications. In particular, we focus in reducing the number of spatial measurements (which generally represents the bulk of measurement time), but the method can be applied to reduce both spatial and frequency measurements [27], although the resulting spatial-frequency measurement grid can be not necessarily convenient.

The main drawback while considering a three-layered back-ground medium is the need to compute the two refractive points occurring a the wall interfaces. To overcome this issue, an equivalent two-layered model is employed [28]–[29], which allows to resort to the same results derived in [25].

Eventually, the spatial sampling points have to be non-uniformly deployed across the measurement aperture according to a law which depends on the geometrical parameters of the configuration and the wall features. This, in particular, allows to highlight the role of the wall thickness and refractive index on the number and distribution of the spatial sampling points.

The rest of the paper is organized as follows. In Section II, in order to make the paper self-contained we briefly report the sampling approach for a general back-ground medium. In Section III, the case of a three-layered medium is considered and the equivalent two.layered medium is employed to quantitatively estimate the spatial sampling points. Section IV to numerically check the sampling scheme. In this section we consider the effect of the wall parameters. Finally, conclusions are briefly summarize the paper.

II. SAMPLING STRATEGY

Consider a 2D scalar geometry invariant along the y-axis. For example look at the one sketched in Fig. 1, which refers to a usual (though simplified) through the wall imaging scene with a three layered background medium.

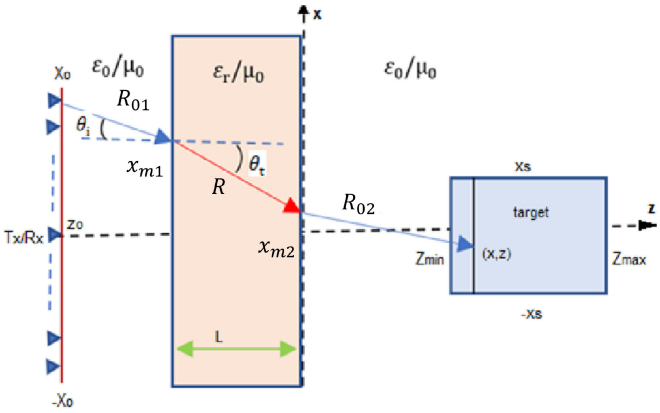

FIGURE 1. Geometry of the problem.

The incident field is radiated by an y-polarized line source at different frequencies; say $\Omega_k = [k_{min}, k_{max}]$ the corresponding band within which the free-space wavenumber k_0 varies. A monostatic configuration is considered, so that the scattered field is collected at the same position as the source while the latter moves (or is deployed) along the segment $OD = [-X_0, X_0]$ of the x-axis located at z_o in the first layer. The targets are assumed to reside within a rectangular region $SD = [-X_s, X_s] \times [z_{min}, z_{max}]$.

Under the Born approximation, the mathematical relationship linking the scattered field E and the unknown object is given by the following linearized scattering operator

$$E(x_o, k_0) = jk_0^2\omega\mu_0 \int_{SD} d\boldsymbol{r} G^2(x_o, \boldsymbol{r}, k_0)\chi(\boldsymbol{r}) \tag{1}$$

with $(x_o, k_0) \in \Sigma = \Omega_k \times OD$ and $\boldsymbol{r} = (x, z) \in SD$. The function $\chi(\boldsymbol{r}) = (\epsilon_s(\boldsymbol{r}) - \epsilon_0)/\epsilon_0$ is the so-called contrast function, with ϵ_s being the dielectric permittivity of the unknown scatterer. The function $G(x_o, \boldsymbol{r}, k_0)$ is the Green function pertinent to the considered background medium.

When the observation domain and the target domain are sufficiently separated (few wavelenghts), than $G(x_o, \boldsymbol{r}, k_0)$ can be asymptotically approximated as

$$G(x_o, \boldsymbol{r}, k_0) \approx \sqrt{h(x_o, \boldsymbol{r}, k_0)} e^{-jk_0\phi(x_o, \boldsymbol{r})} \tag{2}$$

where $\sqrt{h(x_o, \boldsymbol{r}, k_0)}$ is the relevant amplitude factor, and $\phi(x_o, \boldsymbol{r})$ is the phase term that takes into account the propagation path the wave experiences from the target point $\boldsymbol{r} = (x, z)$ to the field point $\boldsymbol{r}_o = (x_o, z_o)$. Accordingly, the scattering model can be rewritten as

$$E(x_o, k_0) \simeq jk_0^2\omega\mu_0 \int_{SD} d\boldsymbol{r} h(x_o, \boldsymbol{r}, k_0) e^{-j2k_0\phi(x_o, \boldsymbol{r})} \chi(\boldsymbol{r}) \tag{3}$$

which in operator notation is written as

$$\mathcal{A} : \chi \in L^2(SD) \rightarrow E \in L^2(\Sigma) \tag{4}$$

where $\mathcal{A}$ is the integral operator in (3) assumed to act between Hilbert spaces of square integrable functions.

In order to devise a sampling scheme for the scattered field a couple of crucial points need to be first addressed.

First, it is noted that $\mathcal{A}$ is not a band-limiting projector. However, it exhibits a well-behaved kernel function which, far from its singularity (which here does not occur because *SD* and *OD* are disjoint), is analytic. This, along with *SD* is bounded, entails that $\mathcal{A}$ is compact. Hence, its range (i.e., the set of possible scattered fields) has an "effective" finite dimension [30]. Accordingly, a finite semi-discrete (where discretization is achieved only for the scattered field space) approximation of (3) can be looked for.

Second, a suitable criterion has to be chosen to guide the sampling scheme that at the same time can be used to assess how the resulting discrete problem approximates the original (continuous) one. For an imaging problem, it is natural to set the sampling scheme so to have (if possible) the same performance in the reconstruction as in the continuous case. Of course, this is in principle possible because the properties of the scattering operator mentioned above and the unavoidable presence of noise that corrupts field measurements.

Here we exploit the same approach as developed in [24] and [25]. More in detail, say

$$\mathcal{B} : E \in L^2(\Sigma) \rightarrow \hat{\chi} \in L^2(SD) \tag{5}$$

a reconstruction operator, that starting from data returns an estimation of the unknown contrast

$$\hat{\chi}(\boldsymbol{r}) = (\mathcal{B}E)(\boldsymbol{r}) \tag{6}$$

Since, the imaging problem is cast as an inverse linear problem, the unknown χ and its reconstructed version $\hat{\chi}$ results linked as

$$\hat{\chi}(\boldsymbol{r}) = \int_{SD} d\boldsymbol{r}' psf(\boldsymbol{r}, \boldsymbol{r}')\chi(\boldsymbol{r}') \tag{7}$$

where $psf(\boldsymbol{r}, \boldsymbol{r}')$ is the inversion scheme point-spread function (psf), i.e., the kernel function of $\mathcal{BA}$. Equation (7) highlights that the contrast function, during the reconstruction process, undergoes a filtering dictated by the psf, a well known fact. Accordingly, the sampling scheme is looked for as the one which allows to approximate the "ideal" point-spread function, i.e., the one obtained when data are continuously collected over the frequency band and the measurement domain.

In general, the point-spread function depends on the scheme adopted to achieve the inversion of the scattering operator. Most inversion operators are in a form of weighted adjoint of the scattering operator. Indeed, they attempt to achieve focusing in the scatterer region by compensating the phase term and possibly equalizing the amplitude term [31]–[33]. Here, we just consider the actual adjoint, $\mathcal{A}^\dagger$, of the scattering operator, that is

$$\mathcal{A}^\dagger : E \in L^2(\Sigma) \rightarrow \hat{\chi} \in L^2(SD) \tag{8}$$

so that the reconstruction is obtained as

$$\hat{\chi}(\boldsymbol{r}) = \left(\mathcal{A}^\dagger E\right)(\boldsymbol{r}) \tag{9}$$

which yields the psf as

$$psf(\boldsymbol{r}, \boldsymbol{r}') \approx \int_\Sigma dk_0 dx_o A(x_o, \boldsymbol{r}, \boldsymbol{r}', k_0) \times e^{2jk_0[\phi(x_o,\boldsymbol{r})-\phi(x_o,\boldsymbol{r}')]} \tag{10}$$

where $A(x_o, \boldsymbol{r}, \boldsymbol{r}', k_0) = [k_0^2\omega\mu_0]^2 h^*(x_o, \boldsymbol{r}, k_0)h(x_o, \boldsymbol{r}', k_0)$, with * denoting conjugation operator.

Using $\mathcal{A}^\dagger$ to approximate the inverse operator has the merit that the corresponding psf actually coincides with the kernel function of $\mathcal{A}^\dagger\mathcal{A}$, and hence can be used to numerically compute the singular spectrum of the scattering operator. The latter, in turns, is of crucial importance while adopting a regularized inverse filtering scheme to achieve the reconstruction. Moreover, since the singular value of $\mathcal{A}$ presents an abrupt decay beyond a critical index (the so-called number of degrees of freedom, NDF [19]–[22]), (10) generally returns a good approximation of the psf that a regularized inverse filtering method would yield (unless a very high unfeasible signal to noise ratio is available). Indeed, the number of sampling points is actually linked to the NDF.

In this paper we are mainly concerned with the spatial sampling. Therefore, wavenumber is sampled by employing standard arguments based on the range extent of the area to be imaged, that is $\Delta k_0 = \pi/(z_{max} - z_{min})$; denote as $k_{0l} = k_{0min} + (l-1)\Delta k_0$ the corresponding sampled frequencies. Hence, (10) is approximated as

$$psf(\boldsymbol{r}, \boldsymbol{r}') \approx \Delta k_0 \sum_l \int_{OD} dx_o A(x_o, \boldsymbol{r}, \boldsymbol{r}', k_{0l}) \times e^{2jk_{0l}[\phi(x_o,\boldsymbol{r})-\phi(x_o,\boldsymbol{r}')]} \tag{11}$$

Thus, determining the spatial sampling is equivalent to finding the spatial positions over *OD* that allows to approximate the spatial integral appearing in (11). In particular, we consider such an integral for $k_0 = k_{0max}$ and $z = z_{min}$, which is expected to be more critical to approximate. This can be roughly justified by observing that the exponential term becomes more oscillating as k increases, while for $z = z_{min}$ the angular sector under which an observation point is "seen" from the investigation domain (which affects the local bandwidth) is larger (see Fig. 2).

Accordingly, we focus on

$$psf_{k_{0max}}(x, x') = \int_{OD} dx_o A(x_o, x, x', k_{0max}) \times e^{2jk_{0max}[\phi(x_o,x)-\phi(x_o,x')]} \tag{12}$$

where the subscript in the right-hand term means that $k_0 = k_{0max}$ and the integrand depends only on x and x' since $z = z_{min}$. Now, by introducing the monotonic increasing transformation

$$\eta(x) = \phi(-X_0, x) - \phi(X_0, x) \tag{13}$$

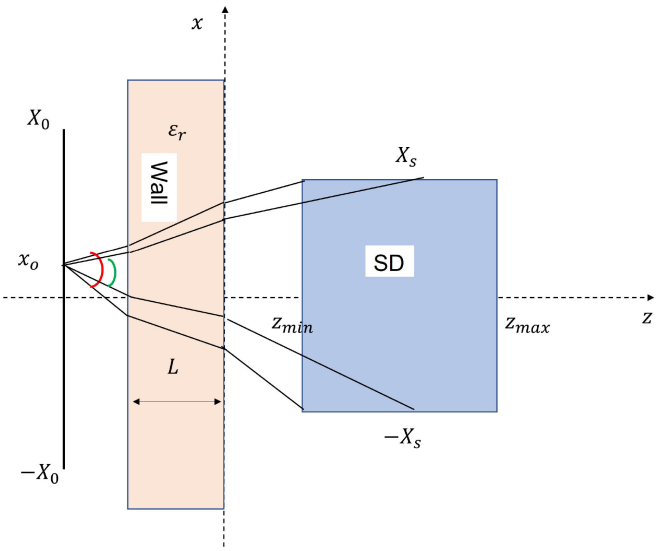

FIGURE 2. Pictorial view on how the local band changes in terms of the depth *z*.

that maps the interval $[-X_s, X_s]$ into $[\eta(-X_s), \eta(X_s)]$, the phase term can be written as

$$2k_{0max}[\phi(x_o, \eta_2) - \phi(x_o, \eta_1)]k_{0max}(\eta_2 - \eta_1)w(\eta_2, \eta_1, x_o) \tag{14}$$

with

$$w(\eta_2, \eta_1, x_o) = 2\int_0^1 \frac{\partial\phi(x_o, x(\eta))}{\partial\eta}\bigg|_{\eta=\eta_1+v(\eta_2-\eta_1)} dv \tag{15}$$

and $\eta_2 = \eta(x)$, $\eta_1 = \eta(x')$. As shown in [25], $w(\eta_2, \eta_1, x_o)$ is a continuous monotonic decreasing function with respect to x_o $\forall\eta_2, \eta_1$. Thus, upon defyining

$$\Omega_w(\eta_2, \eta_1) = \frac{w(\eta_2, \eta_1, -X_0) - w(\eta_2, \eta_1, X_0)}{2} = 1 \tag{16}$$

$$w_{avg}(\eta_2, \eta_1, X_0) = \frac{w(\eta_2, \eta_1, -X_0) + w(\eta_2, \eta_1, X_0)}{2} \tag{17}$$

and $w = \bar{w} + w_{avg}$, (12) can be rewritten as

$$psf_{k_{0max}}(\eta_2, \eta_1) \approx e^{jk_{0max}w_{avg}[\eta_2-\eta_1]} \int_{-1}^{1} K(\bar{w}, \eta_1, k_{0max}) \times e^{jk_{0max}\bar{w}[\eta_2-\eta_1]}d\bar{w} \tag{18}$$

where $K(\bar{w}, \eta_2, \eta_1, k_0) = -A(x_o(\bar{w}), \eta_2, \eta_1, k_0)\frac{dx_o}{d\bar{w}}$ and in (18) we approximated $K(\bar{w}, \eta_2, \eta_1, k_0) \approx K(\bar{w}, \eta_1, \eta_1, k_0) = K(\bar{w}, \eta_1, k_0)$, because the leading order contribution occurs for $\eta_2 - \eta_1 = 0$ [34].

It is assumed to collect the data over a set of spatial positions so that $\bar{w}$ results uniformly sampled. Say $\Delta\bar{w} = \Delta w = w_n - w_{n+1} = w(\eta_2, \eta_1, x_{on}) - w(\eta_2, \eta_1, x_{on+1})$ the corresponding sampling step, with x_{on} being the sampling point in the original observation variable x_o. Then,

$$psf_{k_0}(\eta_2, \eta_1) \approx e^{jk_0w_{avg}[\eta_2-\eta_1]}\Delta w \times \sum_n K(\bar{w}_n, \eta_1, k_0)e^{jk_0n\Delta\bar{w}[\eta_2-\eta_1]}. \tag{19}$$

Now, according to the arguments reported in the Appendix, the sampling in $\bar{w}$ which allows to approximate the point-spread function corresponds to collect the data with a uniform step of π in the variable

$$\zeta(x_o) = k_{0max}[\phi(x_{on}, -X_s) - \phi(x_{on}, X_s)]. \tag{20}$$

In particular, eq. (20) entails to non-uniformly sample the observation variable x_o.

III. SAMPLING FOR A TWI SCENARIO

Previous arguments are completely general. Here, we particularize them to the case of a TWI scenario characterized by a three-layered background medium (see Fig. 1). In this case, the targets are hidden behind a wall represented by a layer having thickness L and relative dielectric permittivity ϵ_r, which are assumed known. The first and third layers are instead free-space with dielectric permittivity denoted as ϵ_0. The magnetic permeability is everywhere the one of the free-space μ_0. While k_0 is the free-space wavenumber, $k_b = nk_0$, with $n = \sqrt{\epsilon_r}$ being the refractive index, denotes the wavenumber in the wall layer. For the case at hand, the Green function enjoys the following spectral representation

$$G(x_o, \boldsymbol{r}, k_0) = \frac{-j}{4\pi}\int_{-\infty}^{\infty} dk_x T(k_x) \times e^{-jk_{zb}L}e^{jk_{z0}(L+z_o-z)}e^{-jk_x(x_o-x)} \tag{21}$$

with k_x being the spectral variable,

$$k_{z0} = \begin{cases} \sqrt{k_0^2 - k_x^2} & \text{if} \quad k_x \le k_0 \\ -j\sqrt{k_x^2 - k_0^2} & \text{if} \quad k_x > k_0 \end{cases}$$

$$k_{zb} = \begin{cases} \sqrt{k_b^2 - k_x^2} & \text{if} \quad k_x \le k_b \\ -j\sqrt{k_x^2 - k_b^2} & \text{if} \quad k_x > k_b \end{cases}$$

and the transmission coefficient $T(k_x)$ given by

$$T(k_x) = \frac{1 - \Gamma.^2}{k_{z0}\left(1 - \Gamma.^2 e^{-2jk_{zb}L}\right)} \tag{22}$$

with

$$\Gamma = \frac{k_{zb} - k_{z0}}{k_{zb} + k_{z0}}. \tag{23}$$

This expression is used to compute the synthetic data. However, for the sampling scheme derivation purposes the Green function asymptotic expression is employed. In particular, for the case at hand the phase term is given by

$$\phi(x_o, \boldsymbol{r}) = R_{01} + R_{02} + nR \tag{24}$$

with

$$R_{01} = \sqrt{(x_{m1}(x_o, \boldsymbol{r}) - x_o)^2 + (L + z_o)^2} \tag{25}$$

$$R_{02} = \sqrt{(x - x_{m2}(x_o, \boldsymbol{r}))^2 + z^2} \tag{26}$$

being the two paths traveled by the waves in free-space whereas

$$R = \sqrt{(x_{m2}(x_o, \boldsymbol{r}) - x_{m1}(x_o, \boldsymbol{r}))^2 + L^2} \tag{27}$$

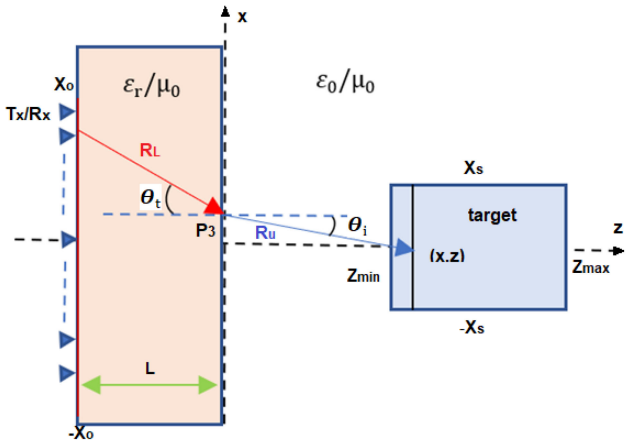

FIGURE 3. Equivalent two-layer model.

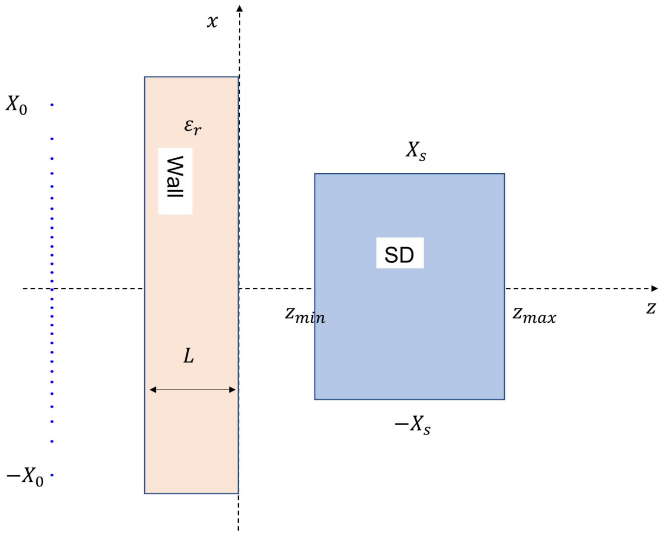

FIGURE 4. Non-uniform distribution of x_o. The configuration parameters are set to $X_s = 0.7m$, $z_{min} = 0.2m$, $z_{max} = 1.2m$, $k_{min} = 6.67\pi m^{-1}$, $k_{max} = 10.67\pi m^{-1}$, $X_0 = 1m$, $z_o = -0.5m$, $L = 20cm$ and $n = 3$.

takes into account the propagation inside the wall (see Fig. 1), and $x_{m1}(x_o, \boldsymbol{r})$ and $x_{m2}(x_o, \boldsymbol{r})$ are the refraction points which, according to the Snell's law, are given by

$$\frac{x_{m1} - x_o}{R_{01}} = n\frac{x_{m2} - x_{m1}}{R} = \frac{x - x_{m2}}{R_{02}}. \tag{28}$$

The sampling points can then be determined by solving for eq. (20) once the previous phase function is considered. However, while doing this, one has to compute and to take into account for two refractive points in the phase term of (2). In order to avoid this drawback, an equivalent two-layered model (see (3)) can be employed [28]. This allows to re-express the phase term in (2) in terms of only one refraction point x_{m3} that is

$$\phi(x_o, \boldsymbol{r}) = nR + R_0 \tag{29}$$

where

$$R = \sqrt{(x_{m3} - x_o)^2 + L^2}$$
$$R_0 = \sqrt{(x - x_{m3})^2 + (z_{min} - L - z_o)^2}.$$

and x_{m3} fulfills

$$\frac{x - x_{m3}}{R_0} = n\frac{x_{m3} - x_o}{R}. \tag{30}$$

By introducing this equivalent two-layered re-formulation, the phase term is clearly the same as the three-layered Green function, but the amplitude term is not. However, as discussed above, what matters in determining the sampling point distribution is just the phase term; the amplitude term introduces a different weighing on the spectral component of the actual contrast function $\chi(\boldsymbol{r}')$ resulting in a different structure of the *psf*'s lobes. Accordingly, the same approach developed in [25] can be pursued. Then, it follows that in order to approximate $psf(\boldsymbol{r}, \boldsymbol{r}')$, the spatial measurement positions arise by uniformly sampling the new variable ζ, depending on the configuration parameters,

$$\begin{aligned}\zeta(x_o) = k_{max}\Big[&n\sqrt{(x_o - f_1)^2 + L^2} \\ &+ \sqrt{(f_1 + X_s)^2 + (z_{min} - L - z_o)^2} \\ &- n\sqrt{(x_o - f_2)^2 + L^2} \\ &- \sqrt{(f_2 - X_s)^2 + (z_{min} - L - z_o)^2}\Big]\end{aligned} \tag{31}$$

where f_1 and f_2 is the refraction point, obtained by the Snell's law, corresponding to extreme points in the investigation domain, that is

$$f_1 = x_{m3}(x_o, -X_s)$$
$$f_2 = x_{m3}(x_o, X_s).$$

Since the non-linear relationship between ζ and x_o, uniform sampling in ζ becomes non-uniform in x_o. Accordingly, let Δx_o be the sampling step in x_o, its expression in terms of configuration parameters is given by solving the following equation

$$\zeta(x_o) - \zeta(x_o + \Delta x_o) = \frac{\pi}{\alpha} \tag{32}$$

in terms of Δx_o, with $\frac{\pi}{\alpha}$ the sampling step in ζ and $\alpha \geq 1$ a slight oversampling factor which according to [25] can be chosen equal to $\alpha = 1.1$. Hence, the required number of non uniform spatial samples falling within OD (which, since the mapping in (31) corresponds to the interval $[-\zeta(X_0), \zeta(X_0)]$) turns to be

$$N = \frac{2k_{max}\alpha\zeta(X_0)}{\pi}.$$

In Fig. 4, an example of the measurement points returned by applying the proposed approach is shown. As can be seen,

the points are non-uniformly arranged across the measurement domain; the sampling step is quite constant and lower at the center of the measurement domain and it increases as the observation point approaches the edges. What is more, as shown in [25], the number of sampling points is much lower than the one returned by a half-wavelength sampling or other approaches present in literature [35].

This non-uniform distribution is typical for near field configuration and has already been observed for the homogeneous case. However, compared to the homogeneous case, the way in which the number of sampling points and their non-uniform distribution is affected by the configuration parameters is different. In particular, they are affected by the wall parameters L and ϵ_r. In the next section, an analysis on how the wall affects the sampling grid is performed.

IV. NUMERICAL ANALYSIS

In this section, in order to check the capability of the proposed sampling scheme in approximating the exact point spread function *psf*, some numerical examples are considered. In each example, the exact point spread function *psf* and the one obtained by the proposed sampling scheme are compared. The exact point spread function *psf* is evaluated numerically with a very fine and uniform grid of spatial points within *OD*. Instead, when the proposed non-uniform sampling strategy is considered, the point-spread function is evaluated by

$$psf_e(\boldsymbol{r},\boldsymbol{r}') = \sum_{l=1}^{N_k}\sum_{m=1}^{N}\Delta k_0\left[k_{0l}^2\omega_l\mu_0\right]^2 G^2(x_{om},\boldsymbol{r}',k_{0l}) \times G^{2*}(x_{om},\boldsymbol{r},k_{0l})\frac{dx_o}{d\zeta}|_{x_o=x_{om}}\Delta\zeta \qquad (33)$$

with N_k the number of frequencies within Ω_k collected with an uniform step equal to $\Delta k_0 = \pi/(z_{max}-z_{min})$, $\Delta\zeta = \pi$ and where $\frac{dx_o}{d\zeta}$ is due to the change of variable from x_o to ζ, introduced in order to approximate the integral in x_o of (10). In particular, while computing both the point-spread functions, the exact spectral Green function expression (reported in the previous section) is employed. The approximated Green function introduced in (2) has been employed only to derive the sampling scheme.

Now, in order to appreciate the role of the wall parameters, L and ϵ_r, three representative numerical examples are reported. In particular, they are addresses as

- case 1, $L = 20cm$ and $n = 3$
- case 2, $L = 50cm$ and $n = 3$
- case 3, $L = 20cm$ and $n = 4$

Note that in passing from case 1 to 2, the wall thickness increases, instead from case 1 to 3 the relative dielectric constant increases. For all these examples, the other configuration parameters are set to $X_s = 0.7m$, $z_{min} = 0.2m$, $z_{max} = 1.2m$, $k_{min} = 6.67\pi m^{-1}$, $k_{max} = 10.67\pi m^{-1}$, $X_0 = 1m$ and $z_o = -0.5m$. Finally, the point-spread function corresponding to a point-like target located at $\boldsymbol{r}' = (0.5, 0.5)m$ is considered.

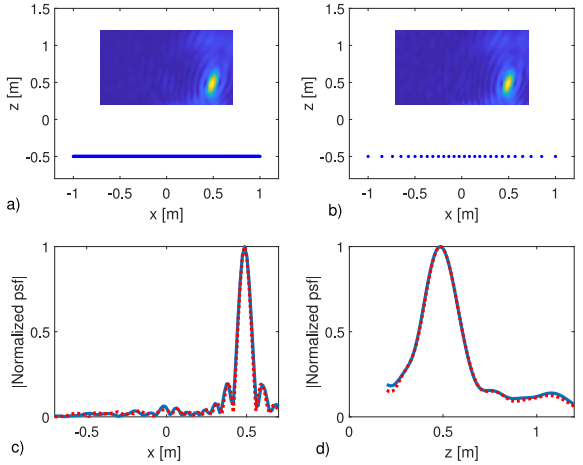

FIGURE 5. Illustrating the normalized point-spread function amplitudes for case 1. Panel a) shows the normalized *psf* and the spatial sampling strategy exploited to achieve its estimation; panel b) the normalized psf_e and the non uniform spatial sampling strategy exploited to achieve its estimation; panel c) and d) the cut-views along x and z, in particular the blue and red lines refer *psf* and psf_e, respectively. $|C(\boldsymbol{r}')| = 0.98$ and $N = 28$.

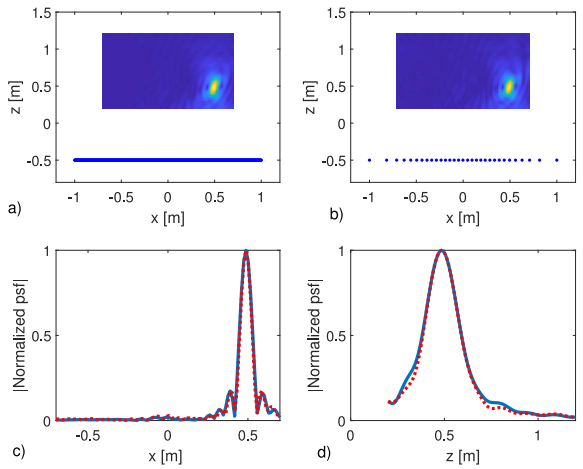

FIGURE 6. Illustrating the normalized point-spread function amplitudes for case 2. Panel a) shows the normalized *psf* and the spatial sampling strategy exploited to achieve its estimation; panel b) the normalized psf_e and the non uniform spatial sampling strategy exploited to achieve its estimation; panel c) and d) the cut-views along x and z, in particular the blue and red lines refer *psf* and psf_e, respectively. $|C(\boldsymbol{r}')| = 0.98$ and $N = 31$.

The corresponding normalized point-spread functions are shown in Figs. 5–7. In each figure, it is shown: the normalized *psf* and the spatial sampling strategy exploited to achieve its estimation (panel a); the normalized psf_e and the non-uniform spatial sampling strategy exploited to achieve its estimation (panel b); the cut-views along x and z, in particular the blue and red lines refer to *psf* and psf_e, respectively. Moreover, in order to quantify how psf_e is close to *psf*, in each figure we report the value of the the correlation coefficient given by

$$C(\boldsymbol{r}') = \frac{\int_{SD} psf_e(\boldsymbol{r},\boldsymbol{r}')psf^*(\boldsymbol{r},\boldsymbol{r}')d\boldsymbol{r}}{\|psf_e\|(\boldsymbol{r}')\|psf\|(\boldsymbol{r}')} \qquad (34)$$

where $\|psf_e\|(\boldsymbol{r}')$ and $\|psf\|(\boldsymbol{r}')$ are the norms computed with respect to $\boldsymbol{r}$ and hence remain function of $\boldsymbol{r}'$. As can be seen,

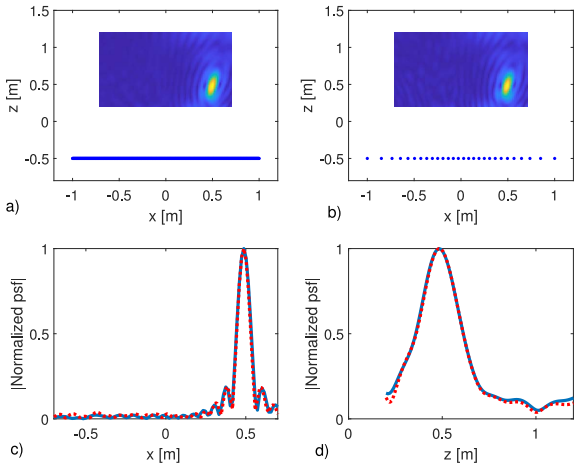

FIGURE 7. Illustrating the normalized point-spread function amplitudes for case 3. Panel a) shows the normalized *psf* and the spatial sampling strategy exploited to achieve its estimation; panel b) the normalized psf_e and the non uniform spatial sampling strategy exploited to achieve its estimation; panel c) and d) the cut-views along x and z, in particular the blue and red lines refer *psf* and psf_e, respectively. $|C(r')| = 0.98$ and $N = 28$.

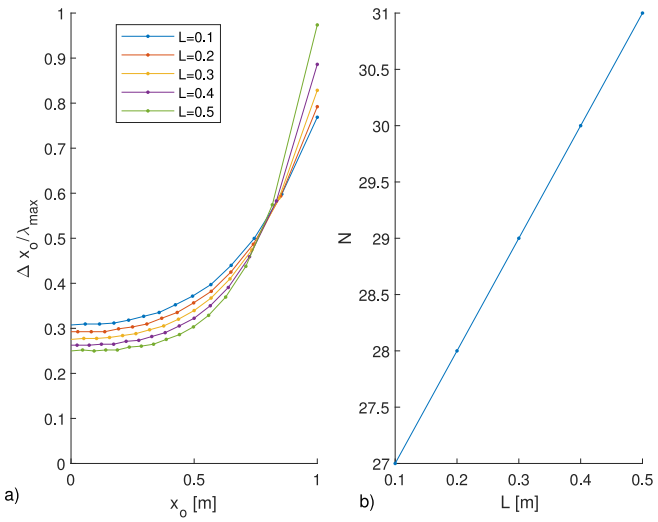

FIGURE 8. Illustration of the wall thickness impact on sampling step (panel a)) and on the number of samples (panel b)). The parameters are $X_S = 0.7m$, $z_{min} = 0.2m$, $z_{max} = 1.2m$, $k_{min} = 6.67\pi m^{-1}$, $k_{max} = 10.67\pi m^{-1}$, $X_0 = 1m$, $z_O = -0.5m$, $n = 3$ and $L \in \{0.1, 0.2, 0.3, 0.4, 0.5\}m$.

psf and psf_e practically always overlap, in fact, the value of C is always very high (i.e., ≈ 0.98). This means that the proposed spatial sampling strategy works very well in estimating the point-spread function for all the considered wall parameters (indeed, this always holds true also for other wall parameters, not reported herein).

Now it interesting to establish how the wall parameters affect the non-uniform sampling point distribution. To this end, Fig. 8 shows the impact of the wall thickness L on the sampling step Δx_o (panel a) and on the number of samples N, by considering a fixed wall refractive index $n = 3$. In the first panel, Δx_o is shown as a function of the observation variable x_o as L ranges among $\{0.1, 0.2, 0.3, 0.4, 0.5\}$ m. As expected, according to the non-uniform observation point distribution,

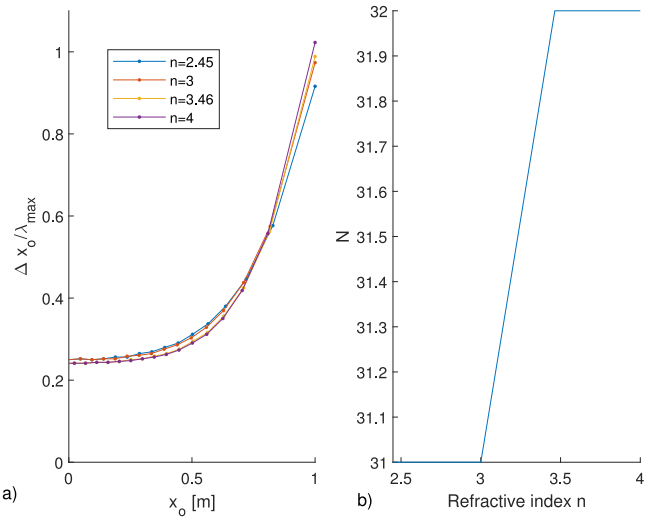

FIGURE 9. Illustration of the wall refractive index impact on sampling step (panel a)) and on the number of samples (panel b)). The parameters are $X_S = 0.7m$, $z_{min} = 0.2m$, $z_{max} = 1.2m$, $k_{min} = 6.67\pi m^{-1}$, $k_{max} = 10.67\pi m^{-1}$, $X_0 = 1m$, $z_O = -0.5m$, $n = \{\sqrt{6}, 3, \sqrt{12}, 4\}$ and $L = 0.5m$.

Δx_o is not constant with x_o, but it is smaller at the center and increases at the edges of the observation domain. Moreover, while passing from low to large value of L, the gap between Δx_o at the center and at the edges increases. Moreover, as L increases, the distribution of sampling points tend to become more uniform at the center and more non-uniform at the edges. By considering, the panel (b) of the same figure, it is evident that the number of sampling points increases as L increases.

Fig. 9 shows instead the impact of the wall refractive indexes n having fixed the wall thickness at $L = 0.5$m. As can be seen, the trend is similar to the previous case. However, compared to the thickness, the refractive index affect is much more weak.

Eventually, it can be concluded that the sampling points are non-uniformly arranged across the measurement domain. The sampling step is quite constant and lower at the center of the measurement domain and it increases as the observation point approaches the edges. This trend is enhanced as the wall thickness and/or n increase. What is more, the derived analytical results works well in predicting the number and the locations of the measurement point according to the wall features.

V. CONCLUSION

In this paper, a strategy to spatially sample the scattered field data in the framework of through-the wall radar imaging has been presented. The approach is conceived so that the point-spread function of the corresponding to semi-discrete problem approximates well the ideal one, that is the one obtained in the case data are continuously collected over the measurement domain. The approach presented in [25] has been followed and adapted to the TWI scenario.

It was shown that the spatial measurements should be deployed non-uniformly across the measurement domain.

More in detail, the obtained analytic results highlight the role of the geometrical parameters of the configuration as well as of the wall thickness L and refractive index n. on the sampling point distribution and on number of samples N has been analyzed. In particular, the refractive index affects less significantly the sampling point distribution. In any case, a further numerical analysis (do not shown here, for brevity) was performed. Basically, the psf at different n belonged to the interval $[2.8 - 3.2]$ was obtained by retaining the sampling corresponding to $n = 3$. The results confirmed that the sampling strategy weakly depends on n. Summarizing, if the electromagnetic features of the wall are not known, they can be estimated someway, and in any case the proposed sampling scheme weakly depends on the wall dielectric permittivity. In this paper, the sampling strategy was derived under the hypothesis of lossless walls. However, if walls with losses are considered, it is expected that the proposed sampling scheme still works in approximating the point-spread function. This is because losses tend to reduce the data spatial bandwidth and hence, the present sampling in some sense oversamples the data. Note that considering losses in the derivation of the sampling scheme would lead to further reduction in the required data. In fact, they require to slightly modify the derivation of the variable parametrization (upon which the sampling is based) and to deal with some related math difficulties. This will be addressed in a future contribution.

APPENDIX

In this Appendix, we establish how to choose the sampling step Δw and the corresponding sampling in x_o. To this end, re-write (19) as

$$psf_{k_{0max}}(\eta_2, \eta_1) = \sum_n \Delta w K(\bar{w}_n, \eta_1, k_{0max}) e^{jnu(\eta_2, \eta_1)} \quad (35)$$

with $u(\eta_2, \eta_1) = k_{0max}\Delta w[\eta_2 - \eta_1]$. Equation (35) is periodic $u(\eta_2, \eta_1)$ with period 2π. Hence, Δw should be chosen so that $psf_{k_{0max}}$ runs over one single period when η_2 and η_1 vary in $[\eta(-X_s), \eta(X_s)]$. These are the same arguments invoked for avoiding greeting lobes in array antenna theory [36]. Note that the most critical situation occurs for $\eta_2 = \eta(X_s)$ and $\eta_1 = \eta(-X_s) = -\eta(X_s)$. Hence,

$$u(\eta(X_s), \eta(-X_s)) = 2\eta(X_s)k_{0max}\Delta w < 2\pi \quad (36)$$

from which results

$$\Delta w = w(\eta(X_s), -\eta(X_s), x_{on}) - w(\eta(X_s), -\eta(X_s), x_{on+1}) < 2\pi \quad (37)$$

with $x_{on} < x_{on+1}$ being two consecutive sampling points in x_o. Now, by using (15) to express $w(\eta(X_s), -\eta(X_s), x_{on})$ and $w(\eta(X_s), -\eta(X_s), x_{on+1})$ yields

$$k_{0max}\big[\big[\phi(x_{on}, X_s) - \phi(x_{on}, -X_s) - \phi(x_{on+1}, X_s) + \phi(x_{on+1}, -X_s)\big]\big] < \pi \quad (38)$$

so that, eventually, the equation for finding the sampling points x_{on} is

$$k_{0max}[\phi(x_{on}, -X_s) - \phi(x_{on}, X_s)] = n\pi. \quad (39)$$

The latter suggests to collect the data with a uniform step equal to π in the variable $\zeta(x_o) = k_{0max}[\phi(x_{on}, -X_s) - \phi(x_{on}, X_s)]$.

REFERENCES

[1] M. G. Amin, *Through-the-Wall Radar Imaging*. Boca Raton, FL, USA: CRC Press, 2017.

[2] R. Solimene, A. Brancaccio, R. Pierri, and F. Soldovieri, "TWI experimental results by a linear inverse scattering approach," *Progr. Electrom. Res.*, vol. 91, pp. 259–272, Jan. 2009.

[3] F. Ahmad, Y. Zhang, and M. G. Amin, "Three-dimensional wideband beamforming for imaging through a single wall," *IEEE Geosci. Remote Sens. Lett.*, vol. 5, no. 2, pp. 176–179, Apr. 2008.

[4] F. Ahmad, M. G. Amin, and S. A. Kassam, "Synthetic aperture beamformer for imaging through a dielectric wall," *IEEE Trans. Aerosp. Electron. Syst.*, vol. 41, no. 1, pp. 271–283, Jan. 2005.

[5] D. Oloumi and K. Rambabu, "Metal-cased oil well inspection using near-field UWB radar imaging," *IEEE Trans. Geosci. Remote Sens.*, vol. 56, no. 10, pp. 5884–5892, Oct. 2018.

[6] L.-P. Song, C. Yu, and Q. H. Liu, "Through-wall imaging (TWI) by radar: 2-D tomographic results and analyses," *IEEE Trans. Geosci. Remote Sens.*, vol. 43, no. 12, pp. 2793–2798, Dec. 2005.

[7] W. Zhang and A. Hoorfar, "Three-dimensional real-time through-thewall radar imaging with diffraction tomographic algorithm," *IEEE Trans. Geosci. Remote Sens.*, vol. 51, no. 7, pp. 4155–4163, Jul. 2013.

[8] A. Salehi-Barzegar, A. Cheldavi, V. Nayyeri, and A. Abdolali, "A fast diffraction tomography algorithm for 3-D through-the- wall radar imaging using nonuniform fast Fourier transform," *IEEE Geosci. Remote Sens. Lett.*, vol. 19, pp. 1–5, 2022.

[9] F. Ahmad and M. G. Amin, "A noncoherent approach to radar localization through unknown walls," in *Proc. IEEE Conf. Radar*, 2006, p. 7.

[10] Q. Huang, L. Qu, B. Wu, and G. Fang, "UWB through-wall imaging based on compressive sensing," *IEEE Trans. Geosci. Remote Sens.*, vol. 48, no. 3, pp. 1408–1415, Mar. 2010.

[11] M. A. Herman and T. Strohmer, "High-resolution radar via compressive sensing," *IEEE Trans. Signal Process.*, vol. 57, no. 6, pp. 2275–2284, Jun. 2009.

[12] A. S. Barzegar, A. Cheldavi, S. H. Sedighy, and V. Nayyeri, "3-D through-the-wall radar imaging using compressed sensing," *IEEE Geosci. Remote Sens. Lett.*, vol. 19, pp. 1–5, 2022.

[13] E. Candes, J. Romberg, and T. Tao, "Robust uncertainty principles: Exact signal reconstruction from highly incomplete frequency information," *IEEE Trans. Inf. Theory*, vol. 52, no. 2, pp. 489–509, Feb. 2006.

[14] E. J. Candes and M. B. Wakin, "An introduction to compressive sampling," *IEEE Signal Process. Mag.*, vol. 25, no. 2, pp. 21–30, Mar. 2008.

[15] R. Obermeier and J. A. Martinez-Lorenzo, "Sensing matrix design via mutual coherence minimization for electromagnetic compressive imaging applications," *IEEE Trans. Comput. Imag.*, vol. 3, no. 2, pp. 217–229, Jun. 2017.

[16] S. J. Reeves and L. P. Heck, "Selection of observations in signal reconstruction," *IEEE Trans. Signal Process.*, vol. 43, no. 3, pp. 788–791, Mar. 1995.

[17] C. Jiang, Y. C. Soh, and H. Li, "Sensor placement by maximal projection on minimum eigenspace for linear inverse problems," *IEEE Trans. Signal Process.*, vol. 64, no. 21, pp. 5595–5610, Nov. 2016.

[18] J. Wang and A. Yarovoy, "Sampling design of synthetic volume arrays for three-dimensional microwave imaging," *IEEE Trans. Comput. Imag.*, vol. 4, no. 4, pp. 648–660, Dec. 2018.

[19] R. Piestun and D. A. B. Miller, "Electromagnetic degrees of freedom ofan optical system," *J. Opt. Soc. America A*, vol. 17, no. 5, pp. 892–902, 2000.

[20] R. Solimene, M. A. Maisto, G. Romeo, and R. Pierri, "On the singular spectrum of the radiation operator for multiple and extended observation domains," *Int. J. Antennas Propag.*, vol. 2013, Jul. 2013, Art. no. 585238.

[21] R. Solimene, M. A. Maisto, and R. Pierri, "Inverse scattering in the presence of a reflecting plane," *J. Opt.*, vol. 18 no. 2, 2015, Art. no. 025603.
[22] M. A. Maisto, R. Solimene, and R. Pierri, "Metric entropy in linear inverse scattering," *Adv. Electromagn.* vol. 5, no. 2, pp. 46–52, 2016.
[23] M. Bertero, *Linear Inverse and Ill-Posed Problems*. New York, NY, USA: Academic, 1989.
[24] M. A. Maisto, R. Pierri, and R. Solimene, "Spatial sampling in monostatic radar imaging," *IEEE Geosci. Remote Sens. Lett.*, vol. 19, pp. 1–5, 2022.
[25] M. A. Maisto, R. Pierri, and R. Solimene, "Sensor arrangement in monostatic subsurface radar imaging," *IEEE Open J. Antennas Propag.*, vol. 2, pp. 3–13, 2021.
[26] T. Sakamoto, T. Sato, P. J. Aubry, and A. G. Yarovoy, "Ultra-wideband radar imaging using a hybrid of Kirchhoff migration and Stolt F-K migration with an inverse boundary scattering transform," *IEEE Trans. Antennas Propag.*, vol. 63, no. 8, pp. 3502–3512, Aug. 2015.
[27] M. A. Maisto, M. Masoodi, G. Leone, R. Solimene, and R. Pierri, "Scattered far-field sampling in multi-static multi-frequency configuration," *Sensors*, vol. 21, no. 14, p. 4724, 2021.
[28] M. Aftanas, J. Rovnakova, M. Drutarovsky, and D. Kocur, "Efficient method of TOA estimation for through wall imaging by UWB radar," in *Proc. Int. Conf. Ultrawideband*, 2008, pp. 101–104.
[29] T. Jin, B. Chen, and Z. Zhou, "Image-domain estimation of wall parameters for autofocusing of through-the-wall SAR imagery," *IEEE Trans. Geosci. Remote Sens.*, vol. 51, no. 3, pp. 1836–1843, Mar. 2013.
[30] G. Newsam, and R. Barakat, "Essential dimension as a well-defined number of degrees of freedom of finite-convolution operators appearing in optics," *J. Opt. Soc. America A*, vol. 2, no. 11, pp. 2040–2045, 1985.
[31] M. A. Maisto, R. Solimene, and R. Pierri, "Depth resolution in stripcurrent reconstructions in near non-reactive zone," *J. Opt. Soc. America A*, vol. 36, no. 6, pp. 975–982, 2019.
[32] M. T. Bevacqua, T. Isernia, R. Palmeri, M. N. Akinci, and L. Crocco, "Physical insight unveils new imaging capabilities of orthogonality sampling method," *IEEE Trans. Antennas Propag.*, vol. 68, no. 5, pp. 4014–4021, May 2020.
[33] G. Ruvio, R. Solimene, A. D'Alterio, M. J. Ammann, and R. Pierri, "RF breast cancer detection employing a noncharacterized vivaldi antenna and a MUSIC-inspired algorithm," *Int. J. RF Microw. Comput. Aided Eng.*, vol. 23, no. 5, pp. 598–609, 2013.
[34] M. Cheney and R. J. Bonneau, "Imaging that exploits multipath scattering from point scatterers," *Inverse Problems*, vol. 20, no. 5, pp. 1691–1711, 2004.
[35] M. Soumekh, "A system model and inversion for synthetic aperture radar imaging," *IEEE Trans. Imag. Process.*, vol. 1, pp. 64–76, 1992.
[36] C. A. Balanis, *Antenna Theory: Analysis and Design*. New York, NY, USA: Wiley, 2016.